Revised submission

HST/ACS Narrowband Imaging of the Kepler Supernova Remnant[1]

Ravi Sankrit[2,3], William P. Blair[4], Lisa M. Frattare[5], Lawrence Rudnick[6], Tracey DeLaney[7], Ilana M. Harrus[8] and Jessica A. Ennis[5]

ABSTRACT

We present narrowband images of the Kepler supernova remnant obtained with the Advanced Camera for Surveys aboard the Hubble Space Telescope. The images, with an angular resolution of $0.05''$ reveal the structure of the emitting gas in unprecedented detail. Radiative and nonradiative shocks are found in close proximity, unresolvable in ground-based spectra, indicating that the pre-shock medium is highly clumped. The ionization structure, traced by differences in the [O III] to [N II] flux ratio, varies on subarcsecond scales. The variation is due to both differences in shock velocity as well as gradients in the evolutionary stage of the shocks. A prominent complex of knots protruding beyond the boundary of the remnant in the northwest is found to consist of bright radiative knots, connected by arcuate nonradiative filaments. Based on the coincidence of the optical emission with a bright isolated knot of X-ray emission, we infer that this feature is due to a Rayleigh-Taylor finger that formed at the contact discontinuity and overtook the primary blastwave.

Subject headings: supernova remnants: individual(Kepler)

---

[1]Based on observations made with the Hubble Space Telescope.

[2]University of California, Berkeley, Space Sciences Lab, 7 Gauss Way, Berkeley, CA 94720.

[3]Visiting Scientist, Johns Hopkins University

[4]Johns Hopkins University

[5]Space Telescope Science Institute

[6]University of Minnesota, Minneapolis

[7]MIT Kavli Institute

[8]Goddard Space Flight Center

1. Introduction

The Kepler supernova remnant (SNR) is the remnant of SN1604, the most recent supernova in our Galaxy that was definitely observed. (Among Galactic SNRs, Cas A is younger than Kepler, but there are no definitive records of observations of the supernova itself.) Kepler is at a distance of $3.9^{+1.4}_{-0.9}$ kpc (Sankrit et al. 2005). It has a galactic latitude of 6.8° which places it at a distance of about 475 pc off the Galactic plane. The remnant is about 200′ in diameter, and a well defined shell is seen in the radio and the X-ray (DeLaney et al. 2002) as also in the infrared 24μm band (Blair et al. 2007). At all these wavelengths the northern limb is significantly brighter than the southern limb. The contrast is much more pronounced in the optical: there are filaments and knots extending all across the northern limb of the SNR, with the brightest emission coming from a region in the northwest where the supernova blast wave is interacting with dense ambient material, while the southern limb is not seen at all (Blair et al. 1991, henceforth BLV). The only other optical emission is from a few regions of knots and filaments near the projected center of the remnant.

There is a long history of optical studies of Kepler, starting with its identification as the remnant of the 1604 supernova by Baade (1943). Early spectra, confirming the high velocities and the SNR identification were obtained by Minkowski (1943). It was included in the optical atlas of Galactic SNRs by van den Bergh, Marscher & Terzian (1973), wherein the proper motion of the brightest emission was estimated and it was conjectured that the emission was from circumstellar material. A more detailed study of the optical emission from Kepler was carried out by van den Bergh & Kamper (1977) who catalogued several individual knots and followed their brightnesses over several epochs of observation between the 1950s and 1977. They derived the overall expansion velocity of the emitting knots and also found that individual knots changed in brightness over time. Spectra of bright knots in the NW were obtained and analyzed by Dennefeld (1982). He found evidence for high densities and nitrogen overabundance and confirmed that the material was circumstellar rather than interstellar. A comprehensive catalog of the knots was presented by D'Odorico et al. (1986) based on Hα+[N II] images of the remnant. Spectra of the high velocity nonradiative filaments were obtained by Fesen et al. (1989), who found that they were caused by shocks with velocities of 1670–2800 km s^{-1}. Detailed spectrophotometry of both radiative and nonradiative filaments and knots were presented by BLV who found that the bright knots in the NW limb had densities of 2,000–10,000 cm^{-3} and were overabundant in nitrogen. They also confirmed high velocities (1500–2000 km s^{-1}) for the fast shocks giving rise to the nonradiative emission. Bandiera & van den Bergh (1991) revisited the changes in the optical emission of the Kepler SNR by tracing the light curves of several individual knots and features from the earliest epochs (*ca.* 1942) up until 1989. They found evidence for both brightening knots and fading knots, and knots that had brightened and then reached

a plateau.

Optical emission from the Kepler SNR traces, primarily, the interaction between the supernova blastwave and the surrounding medium. Thus, by probing the region in which the supernova explosion took place, optical studies are useful for understanding the nature of the progenitor system. In the case of Kepler, this is particularly important since it is the only one of the six historical SNRs where the supernova type is yet unknown. Originally, Baade (1943) classified it as a Type Ia based on the historical light curve. However, it was shown by Doggett & Branch (1985) that the light curve was not a sufficient discriminant in the case of Kepler. This, along with the identification of dense, nitrogen-rich material (Dennefeld 1982) led to models that explicitly assumed a core-collapse origin for the remnant (Bandiera 1987; Borkowski et al. 1992). More recently, X-ray data (Cassam-Chenaï et al. 2004) and *Spitzer* infrared data (Blair et al. 2007) indicate that Kepler was probably the result of a Type Ia. However this was not unequivocally claimed, and was not conclusively demonstrated. Regardless of what type Kepler eventually turns out to be, models of its evolution will necessarily be informed by, and will have to reproduce the results of optical observations of the remnant.

In this paper we present narrowband optical images of the Kepler SNR obtained with the Advanced Camera for Surveys (ACS) aboard the Hubble Space Telescope (HST). These observations reveal the morphology and ionization structure of the optical emission from Kepler at unprecedented spatial resolution. The observations are described in §2. In §3, we first present an overview of the emission seen in the ACS observations. Then we discuss the distribution of radiative and nonradiative shocks (§3.1) and the small scale ionization structure by considering the [O III] and [N II] emission morphologies (§3.2). In §4 we discuss the complex of knots designated 31/32 by D'Odorico et al. (1986), which are caused by Rayleigh-Taylor like instabilities and are developing on a time scale of about a decade. In §5 we summarize our findings, and conclude with a discussion of the role that these and future high-spatial resolution optical images might play in our overall understanding of Kepler.

2. Observations and Data Processing

Observations of the Kepler SNR were obtained with the ACS Wide Field Camera (WFC) on August 28 and 29, 2003 as part of a Cycle 12 Guest Observer Program (PID 9731). The observations were centered on $\alpha_{J2000}, \delta_{J2000}$ = 17:30:39.58, −21:29:10.1. The ACS/WFC field of view is just sufficient to include all of the optical emission from the Kepler SNR, except for the eastern extremity of the northern limb.

Observations were obtained through the filters F658N, F660N, F502N and F550M. Information about the observations is summarized in Table 1. F658N lets through both Hα 6563Å and [N II] 6584Å line emission, while F660N isolates the [N II] 6584Å emission. F502N lets through [O III] 5007Å line emission. The F550M filter is largely line-free and allows the identification of stars in the crowded field around Kepler. This is important because some of the smallest knots in the SNR could easily be confused with stars in the line filter images.

A standard offset pattern with four individual pointings was implemented for the observations through each of the filters. The pattern consists of integer pixel dithers that allow the removal of hot pixels and a standard dither so that there is no loss of field coverage due to the ACS/WFC chip gap. Each pointing was split into two exposures for cosmic ray removal. The exposures through each of the filters were combined using the MultiDrizzle package (Koekemoer et al. 2002). In addition to cosmic ray rejection and hot pixel removal the program corrects the geometric distortion and produces a final "clean" image. The resulting images are aligned north up and east to the left. The data that we present and analyze are the four MultiDrizzled, aligned images covering a region $\approx 200'' \times 200''$ at a spatial resolution of $0.05''$.

3. Morphology of Optical Emission

The ACS Hα+[N II] image of the Kepler SNR is shown in Fig. 1. The image was produced by subtracting a background-subtracted, scaled F550M continuum image from a background-subtracted F658N image. Overall, the optical emission is sparse. The boxes highlight different emission regions, and are numbered for ease of reference to individual regions and features. The nebular emission consists of a few regions of knots towards the center of the remnant (boxes 1,2 and 3), the bright NW knots (boxes 5 and 6), knots and faint filaments along the northern limb (box 7, extending into 6 and 5), and a few patches of faint emission delineating the Western perimeter (box 4). There is no optical emission from the lower portion of the image - a careful examination shows that all the features are stars that have not been fully subtracted. The distribution and extent of the optical emission within the remnant is best seen by comparing the morphologies in different wavebands. We refer the reader to Fig. 6 of Blair et al. (2007), which shows a three-color composite of the HST Hα image, a 24μm image obtained with the *Spitzer Space Telescope* and an X-ray image obtained with *Chandra*.

These HST/ACS data on Kepler represent an improvement in angular resolution of about a factor of 20 over all previously published optical data. Therefore, these images yield a very different picture of the optical emission when examined at small scales. For

example, features identified as a single knot in ground based images are shown to consist of numerous smaller knots, and these smaller sub-arcsecond scale features often show a diversity of morphologies and ionization structures among themselves. In the following subsections we explore some of the observed properties of the optical knots and filaments seen at high angular resolution. Although the features identified by D'Odorico et al. (1986) cannot be considered single knots anymore, we follow the catalog numbering introduced by them in the following discussion. The numbers (e.g. D49) will refer to the approximate locations marked in Figures 1a and 1c of D'Odorico et al. (1986). Most of the knots D1 to D29 are in box 5 of Fig. 1; the exceptions, D4 and D8, are in box 3. D30 is at the bottom right corner of box 2 and D31,32 and 33 are in box 6. D34 to D45 are in box 2 and the remaining knots, D46 to D64 are distributed between boxes 1 and 7.

3.1. Balmer-dominated Nonradiative Shocks

Shocks are defined to be nonradiative when they are still in the stage where the post-shock gas has not had time to cool radiatively. If the shock is running into material that is partly neutral, collisionally excited Balmer lines of hydrogen are produced in a narrow zone just behind the shock front. The atoms, which are neutral, pass undisturbed through the shock front, but some undergo charge exchange with the hot ions in the post-shock region prior to excitation. Thus, the Balmer lines consist of a narrow component produced by the slow neutrals, and a broad component produced by the fast neutrals (Chevalier, Kirshner & Raymond 1980). The optical emission from these shocks is almost entirely from the Balmer lines, the strongest of which is Hα at 6563Å. These Balmer-dominated nonradiative shocks are readily identified by the characteristic two component Hα emission, and the lack of forbidden line emission from species such as S^+ and N^+ that are characteristic of the brighter radiative shocks.

Nonradiative shocks in Kepler were first identified by Fesen et al. (1989) in optical spectra obtained across two filaments on the northeast and northwest rims. Although these filaments are somewhat more diffuse than the Balmer-dominated shocks in other remnants such as the Cygnus Loop (Hester et al. 1994) and Tycho (Ghavamian et al. 2001), they have a considerable linear extent around the perimeter, and they are significantly fainter than the knots (see Fig. 1, boxes 5 and 7). Subsequently, in an extensive spectrophotometric study of Kepler, BLV confirmed the nonradiative nature of these filaments, but also found evidence for Balmer-dominated emission from more compact, knotty regions, especially towards the projected center of the remnant.

We can distinguish between Balmer-dominated nonradiative shocks and radiative shocks

by comparing the F658N and F660N images. This is illustrated in Fig. 2, where the F658N and F660N filter throughputs are plotted as functions of wavelength. The bandpass of the F658N filter includes the Hα line (6563Å) near its blue edge, and extends up to about 6620 Å (half the peak throughput) at the long wavelength end. The bandpass of the F660N filter is contained entirely within that of the F658N filter, with the [N II] 6584Å line near its blue edge. The throughput of the F660N filter for [N II] emission at the systemic velocity of Kepler, -185 km s^{-1}, is 60% that of the throughput for zero-velocity [N II] emission. It falls to less than 10% only for a velocity of about -600 km s^{-1} (i.e. 6570Å). Therefore, for emission at the systemic velocity of Kepler and up to a velocity of about $+500$ km s^{-1} pure Balmer filaments and knots will be visible in the F658N image but not in the F660N image. Conversely, any emission visible in the F658N image and not in the F660N image will be due to Hα and not [N II]. Hα emission from material at velocities higher than about $+500$ km s^{-1} will be detected in both F658N and F660N images and in such cases it will be impossible to identify Balmer-dominated filaments. Emission at such high red-shifts has not been observed in Kepler, and is probably a negligible contributor in the ACS images. The important point is that the [N II] emission from radiative shocks at these high red-shifts would not be mistakenly identified as pure Balmer emission. Only in the case that the emission is highly blue-shifted will any confusion arise: in that case, the [N II] emission will be captured in the F658N image but not in the F660N image, and perhaps the Hα will have moved out of the F658N bandpass and not be detected at all. Since no [N II] emission at such high blue-shifts has been identified in Kepler to date, we do not expect that this confusion actually occurs.

In Fig. 3 we show a difference image of the NW knots (box 5 in Fig. 1). The field of view is $45.0'' \times 55.0''$. The image is the difference between the background-subtracted F658N image and the background-subtracted F660N image, suitably scaled. The scaling factor, 2.7, applied to the F660N image was such as to make the background average close to zero. In the difference image, all the Balmer-dominated emission is white, and all the black regions are radiative. This separation is quite robust since, in this region, the [N II] emission from radiative shocks is typically stronger than the Hα emission (BLV).

The nonradiative emission appears to arise in a continuous band, about $10''$ wide, starting from the upper left and continuing all the way down to the lower right of the image, and it ends in a fan of faint filaments (labeled in Fig. 3). In this region, the southernmost extents of the nonradiative filaments and of the radiative knots are roughly coincident. This suggests that the medium into which the nonradiative shocks are moving is associated with the denser pre-shock gas responsible for the bright radiative knots. For example the pre-shock region may be a cloud that is highly clumped so that large density contrasts occur on small scales. Further exploration of these two issues, (i) the continuity of the nonradiative filaments and

(ii) the association of the pre-shock media, requires spectroscopic observations of sufficient angular resolution to isolate the emission from Balmer-dominated filaments in the region of bright radiative knots. Imaging observations, and the existing published spectroscopic data are inadequate for these purposes.

In addition to the main band of filaments, there exist two Balmer-dominated features worth noting. The first is labeled "fluff" in Fig. 3 and is a region of patchy, diffuse emission. This may be an example of a radiative shock that is slow enough that it does not produce detectable levels of [N II]. The models of Hartigan et al. (1987) predict that the [N II] to Hα flux ratio falls precipitously below 30 km s^{-1}. The second is a bow-shock shaped feature (inset) with the "head" pointing towards the interior of the remnant; the radiative "tail" is possibly an associated feature. The direction of the bow-shock head suggests that it is a dense clump of material that was overtaken by the primary shock.

We turn now to a consideration of two regions, the first around D49/D50 in the center-east part of the remnant (box 1 in Fig. 1) and the second around D41-45 towards the center of the remnant (box 2 in Fig. 1).

In their spectrophotometric study of Kepler, BLV clearly detected both narrow and broad Hα emission from the D49/D50 region and from the D41,42,44,45 set of knots. They found a slight hint of [N II] emission in the spectrum (see their Fig. 8b) but it was not measurable. In the D41,42,44,45 spectrum, they clearly detected [N II] emission (their Fig. 8d) as well as [S II] emission (their Fig. 7c). BLV recognized the problem of having detected these forbidden lines in a region dominated by nonradiative shock emission but were not able to resolve the issue. More recently, Sollerman et al. (2003) obtained high resolution optical spectroscopy of the D49/D50 region and detected [N II] emission at -185 km s^{-1}, the systemic velocity of Kepler. They suggested that the forbidden line emission occurs in the shock precursor, since the shock velocity ($\sim$ 1000 km s^{-1}) is too high for the production of any [N II] in the post-shock gas. As we show, the small-scale structure of the emitting knots, in conjunction with the exact slit positions while obtaining the spectra, may have a bearing on the interpretation of these results.

In Fig. 4a, we show a 32.5$''$ $\times$32.5$''$ region that includes D49/D50 in the upper-right corner. The star subtracted F658N image is displayed in red, and the star subtracted F660N image in green. The field is dominated by nonradiative shock emission (red) with a few groups of knots that are radiative (red+green is yellow). Fig. 4b shows a 10$''$ $\times$ 12.5$''$ field centered on D49/D50. Here, the F658N and F660N images have not been star-subtracted, and the continuum F550M image is displayed in blue. Thus stars are seen as white dots. Two yellow knots, indicating the presence of [N II] emission are clearly seen: one is on the western side of the 'Λ' shaped feature (Fig. 4c) and the other is an isolated knot about

5" directly west. (The yellow portion on the eastern side of the 'Λ' is an artefact, as seen by its right-angled shape - there are many such features scattered around the ACS/WFC field.) The $3'' \times 3''$ blow-up of the 'Λ' in Fig. 4c highlights the small-scale structure of the emission: the localized [N II] emission knot roughly $0.25'' \times 0.11''$ in extent is prominent, and embedded in a more extensive region of nonradiative emission. Thus, the detection or non-detection of [N II] in lower spatial resolution spectra of D49/D50 would depend crucially on whether these tiny radiative knots were included or not in the spectrograph slit.

Fig. 5 is a 3-color image of a cluster of knots towards the center of Kepler. The field of view shown is $25.0'' \times 17.5''$. The F658N image is in red, the F660N image in green and the F502N image in blue. The images have been background subtracted, and stars have been subtracted using the line-free F660M image. The knots D41,42,44 and 45, nominally those that were included in the BLV spectrum discussed above, are labeled. (Note that D44 refers to the emission included between the two arrowheads.) The exact identification of the other knots in the field is difficult, but together they correspond to the region covered by D36,38,39 and 40 (see Fig. 1c of D'Odorico et al. 1986). In this image, nonradiative shocks are clearly visible in red. Radiative shocks emitting [N II] but not [O III] are yellow, and radiative shocks emitting both [N II] and [O III] are white. We defer discussion of the [O III] emission to the next section. Here we note that the Balmer-dominated shocks and the radiative shocks are interspersed among each other within a small area. The small-scale structure included in the spectrograph slit led to BLV obtaining a spectrum that contained signatures of both nonradiative and radiative shocks.

3.2. [O III] Emission

The ionization energy required to form O^{++} is higher that that required to form N^{+}. Therefore, faster shocks are needed for producing [O III] $\lambda\lambda$4959,5007 emission than for producing [N II] $\lambda\lambda$6548,6584 emission. Model calculations show that [N II] emission arises in shocks as slow as 40 km s^{-1}, but that it requires shock velocities of at least 90 km s^{-1} to produce significant [O III] emission (Hartigan et al. 1987). These calculations predict that for solar abundances the [O III] λ5007 line is stronger than the [N II] λ6584 line when shocks are faster than about 100 km s^{-1}.

[O III] emission was detected in Kepler in the early spectrum of Minkowski (1943), but its line flux was accurately measured only decades later. Dennefeld (1982) obtained a flux-calibrated spectrum of a field in the bright NW region, and found that the line fluxes, including [O III], were typical of a 100 km s^{-1} shock. In their wider ranging spectrophotometric study of Kepler, BLV measured the [O III] flux in several locations. They found

that the observed [O III] λ5007 to [N II] λ6584 flux ratio ranged from 0 to about 0.24 in the radiative knots. The color excess, E_{B-V}, is ≈ 0.9 towards Kepler (BLV). Correcting for reddening based on this value, the maximum observed [O III] to [N II] flux ratio corresponds to an intrinsic intensity ratio of about 0.6. Based on the [O III], [N II], [S II], and Hα line fluxes they measured, BLV concluded that the fastest radiative shocks in Kepler had velocities of about 100 km s^{-1}, and that the nitrogen was at least a factor of 2 overabundant relative to the solar value.

3.2.1. Small-scale structure

There is structure in the [O III] emission on small angular scales in Kepler. We have already encountered an example of this in the knots towards the center of the remnant (Fig. 5). In that image, the regions emitting both [N II] and [O III] are white, while those emitting [N II] but not [O III] are yellow. In the complex of knots designated D44, the knot in the middle is prominently white. The two narrower features just to the NW of this central white knot are yellow. There is a small blob WSW of the white knot and right next to it that appears more bluish. This indicates that the [O III] to [N II] flux ratio is higher in the blob than in the knot. In the string of knots towards the upper right of the image, only two knots, near the lower end show [O III] emission. These variations would have an important bearing on the interpretation of lower spatial resolution spectrophotometry results.

To illustrate this point quantitatively, we discuss the region around D52–55 near the NE limb of the remnant (box 7 of Fig. 1), which contains several knots at subarcsecond scales, some of them prominent [O III] emitters and others not. HST/ACS images of a $6.0'' \times 4.5''$ area in the vicinity of knot D52 are shown in Fig. 6. The F658N image (top panel) shows the overall morphology of the emission, including both Hα and [N II] emission. The star-subtracted F660N image (middle panel) isolates the [N II] emission, which is seen to arise in distinct knots a few arcseconds across in size. The star-subtracted F502N image (bottom panel) shows the [O III] emission, also restricted to small knots, and with a large variation in intensity. Several residuals due to the star subtraction are identified as artefacts from the continuum (F550M) image and are marked with asterisks in the F660N image.

The observed [O III] to [N II] flux ratios for the individual knots exhibit a significant variation. We have quantified this by selecting several small regions based on the F660N image. These regions are shown, and labeled in Fig. 6 (middle panel). The total counts within the regions were converted to fluxes using the following equation from the ACS instrument hand book (version 7.1)

$$R_{filter} = 2.23 \times 10^{12} \times (QT)_\lambda \times \lambda_0 \times F_{line}$$

where R_{filter} is the observed count rate, $(QT)_\lambda$ is the system throughput at the desired wavelength, λ_0 is the rest wavelength of the line in Angstroms, and F_{line} is the line flux in erg s^{-1} cm^{-2}. We calculate the conversion factor for a wavelength corresponding to the rest velocity of Kepler of -185 km s^{-1}. From the plots given in the ACS instrument handbook (Ch. 10), we find that the system throughput is 14% for F660N at 6580Å and 28% for F502N at 5004Å. Using these values in the above equation, we obtain the following expression for the flux ratio:

$$F_{[OIII]}/F_{[NII]} \approx 0.7 \times R_{F502N}/R_{F660N}$$

For the F660N filter, the throughput is a steep function of wavelength around the [N II] line, decreasing with decreasing wavelength (i.e. with greater negative velocities, see Fig. 2). This introduces some uncertainty into the conversion factor in the above relationship.

The observed [O III] to [N II] flux ratios are, for *region 1:* 0.11, *2:* 0.46, *3:* 0.41, *4:* 0.06, *5a:* 0.55, and *5b:* 0.45. Note that region 5a includes just the one knot prominent in [O III] while 5b is a larger region enclosing both knots. Regions 1, 2, 3 and 5a are about 0.125 $arcsec^2$ (50 pixels) and regions 4 and 5b are about 0.225 $arcsec^2$ (90 pixels). At this high angular resolution, we observe [O III] to [N II] flux ratios that are over twice as high as the values measured by BLV. The highest observed ratio, 0.55 corresponds to an intrinsic ratio of about 1.4 for emission from Kepler. These higher ratios could be due to shocks with velocities in excess of 100 km s^{-1}. They could also indicate that the shocks are "incomplete". That is, there has not been sufficient time for the N^+ zone to have formed in the post-shock gas. In either case, our results show that such differences in the shock conditions exist on small angular scales.

3.2.2. Ionization structure in the NW knots

We now turn to the emission from the bright complex of knots in the NW limb of the remnant (box 5 in Fig. 1). In Fig. 7 the [N II] emission, overlaid with [O III] contours is shown in the left panel. Two levels of [O III] emission are displayed by the contours: the faintest emission clearly above the noise (0.005 $counts\ pixel^{-1}\ s^{-1}$), and an approximate middle value for a bright knot (0.09 $counts\ pixel^{-1}\ s^{-1}$). The left panel image shows clearly that wherever there is [O III] emission it is coextensive with the [N II] emission. Furthermore, an examination of the interior contours shows that bright [O III] emission is in every case associated with bright [N II] emission. However, there are a number of features, located primarily towards the interior of the remnant, that are prominent in [N II] but are

not detected in [O III].

The right panel of Fig. 7 shows the flux ratio, $F_{[\mathrm{O\ III}]}/F_{[\mathrm{N\ II}]}$, in reverse-grayscale (darker areas correspond to higher values of the ratio). All pixels with either [O III] or [N II] count rates less than 0.004 *counts pixel*$^{-1}$ s^{-1} were set to zero. [O III] contours are the same as in the left panel. Within most of the clumps, defined by the outer (faint) [O III] contour, there is a gradient in the flux ratio, with higher values closer to the shock front and lower values towards the interior of the remnant. This is particularly evident in the clumps along the eastern edge of the whole complex. The flux ratios lie in the range 0.03–0.5. As in the case of the region around D52 (§3.2.1, above) there are small scale features where the [O III] to [N II] flux ratio is higher than any value measured by BLV.

In order to estimate the properties of the shock structure, we ran a plane-parallel steady shock model calculation using an updated version of the code first presented by Raymond (1979). We used the following input parameters: 80 km s^{-1} shock velocity, 100 cm^{-3} pre-shock hydrogen number density, 1.0μG pre-shock magnetic field, and solar elemental abundances. The downstream properties we are concerned with do not depend on the ionization state of the pre-shock gas, and in our model calculation we assumed it to be fully ionized. The calculation shows that the [O III] and [N II] emission peak at $\approx 2.3 \times 10^{14}$ cm and $\approx 2.6 \times 10^{14}$ cm, respectively, downstream from the shock front. The temperatures at the peak locations are $\sim$ 28000 K and $\sim$ 12000 K respectively, and the hydrogen number densities rise from $\sim$ 1700 cm^{-3} in the [O III] zone to $\sim$ 4200 cm^{-3} in the [N II] zone. The hydrogen column density swept up by the shock between the [O III] peak and the [N II] peak is $\sim 1 \times 10^{17}$ cm^{-2}. For the shock velocity and pre-shock density used, this amount of material is swept up in about 4 years.

At the distance of the Kepler SNR, 3.9 kpc, the ACS/WFC pixel size of 0.05″ corresponds to about 3×10^{15} cm. The width of the shock structure (from the front to the [N II] zone) predicted by the model is less than 1/10 this value. Thus, our calculation shows that the [O III] and [N II] zones for a given shock would be unresolved in ACS/WFC images, and therefore that the [O III] and [N II] emission would be coextensive.

The gradient in the [O III] to [N II] ratio is thus most probably due to O^{++} recombining to O^{+} while clumps of shocked gas detach themselves from the shocked region by way of instabilities. The result is a complex morphology of knots containing N^{+} but where a part or all of the O^{++} has recombined. At temperatures of about 15000 K, the O^{++} to O^{+} recombination timescale is about 3 years for densities of about 2000 cm^{-3} (Nahar 1999). This is (as expected) about the same time as that predicted by the shock model calculation between the development of the peak [O III] emission and peak [N II] emission. The N^{+} to N^{0} recombination timescale is about 15 years under these conditions (Nahar & Pradhan

1997). Thus knots can continue to emit [N II] for several years after their isolation from the shock front. This timescale of about a decade is comparable to the timescale observed for changes in the brightness of knots (Bandiera & van den Bergh 1991).

4. Structure and Development of Knots D31/32

Knots D31 and D32 first appeared on the north-northwestern limb of the Kepler SNR sometime around 1970 (van den Bergh & Kamper 1977). They brightened rapidly and by 1985 were comparable in intensity to the NW knots (D'Odorico et al. 1986). Between 1983 and 1989 they doubled in brightness (Bandiera & van den Bergh 1991). Their light-curves make these knots remarkable enough, and the high angular resolution ACS images reveal their structure in fascinating detail.

In Fig. 1, knots D31 and D32 are found in the right half of box 6. The emission near the left edge of the box is D33. It is less prominent than D31 and D32 but it may be part of the same system of knots. The precise relationship of D33 to the rest of the structure is of secondary importance here, and for convenience we refer to the emitting complex as D31/32. The bright knots in the complex are connected to fainter filaments with a well-defined curvature protruding beyond the nominal boundary of the remnant as defined by the linear nonradiative shocks that lie both to the northeast and the southwest from D31/32. This protrusion is clearly seen both in the radio (DeLaney et al. 2002, the "bump" in their Fig. 2) and in the X-ray (Reynolds et al. 2007, Fig. 1).

The structure of the optical emission can be seen in Fig. 8. The top panel shows the F658N image and the bottom panel shows the F660N image. The narrow curved filaments are seen only in the F658N image indicating pure Hα emission, while the clumpy knots are bright [N II] emitters. As discussed in §3.1, this allows us to identify the narrow filaments as nonradiative shocks and the dense clumps as radiative shocks. Morphologically, the dense clumps constituting D31 and D32 appear to be connected back to cusps between the arcs of Hα emission.

In order to study possible changes in the optical emission of the knots, we compared the Hα+[N II] image obtained in 1987 (and presented by BLV) with the F658N image (Fig. 9). The ACS image was aligned with the Las Campanas image based on star positions, and was smoothed with a gaussian kernel to match the $\sim 1''$ resolution of the ground-based image. Since the absolute photometry was not available, it was necessary to choose a relative scaling between the two images so that real differences could be displayed reliably.

We selected a single knot whose position had not changed ("a" in Fig. 9, right panel)

and multiplied the F658N image by a scale factor so that the total counts in the knot were equal in both datasets. The assumption that the knot brightness has reached a plateau is a reasonable one. The intensity of knot "a" relative to that of the brightest knots in the NW region has remained approximately the same between the two epochs, and Bandiera & van den Bergh (1991) found that many of the bright knots in the NW (e.g. D19) had not increased in luminosity in the 50 years covered by their study. They also found that in no case had any knot brightened and then faded away in the 50 year time period covered by their observations.

In Fig. 9, the three-color images consist of the 1987 Hα+[N II] image in red, the F658N image in green and the F550M continuum image in blue. (The continuum image was also aligned with the ground-based image and smoothed to its resolution.) The image in the left panel has been displayed so as to reveal the fainter emission. The advance of the primary shock (the linear feature at the bottom right of the image) is clearly visible as bands of red and green emission. The curved filaments associated with knots D31/32 have also moved forward: the red and green are well separated.

In the right panel, the display range has been chosen to highlight the changes in the bright regions. Knot "a" is well isolated and has not changed position between the two epochs of observation. As described above, the images have been scaled so as to make its "brightness" equal at both epochs. The two bright knots labeled "b" have also remained stationary and their luminosities have not changed significantly. (Note that there is a star overlapping the knot on the left.) Knot "c" has brightened considerably between 1987 and 2003, and marks one end of the complex of emission. The knot immediately to the left of "c" appears to have either faded or moved so that the distribution of the emission has changed. The feature labeled "d" connects "c" to the arcuate Balmer-dominated filaments (see Fig. 8 top panel). The label "e" refers to the region between the forward shock and the "b" knots. Emission in the region is present in the 2003 image, as seen in the left panel image (and in Fig. 8). It has perhaps become fainter since 1987, or maybe the structure has changed with material getting concentrated in a smaller region as the bright "b" knots detach themselves from the curved, forward moving filaments. The features labeled "f" correspond to knot D33 of D'Odorico et al. (1986). These appear to have increased in brightness between the two epochs. The full-resolution ACS images in Fig. 8 show that "f" is composed of several structures, many less than an arcsecond in size.

Further insight into the physical processes responsible for the D31/32 emission comes from a comparison of the X-ray and optical images. An X-ray image, obtained with *Chandra* of a $51.6'' \times 40.6''$ region around D31/32 is shown in the top panel of Fig. 10. The X-ray data are a 100 ks subset of the *Chandra* Large Program dataset obtained in August 2006

and kindly made available to us by Dr. Stephen Reynolds (NCSU). The image is overlaid with contours that highlight the bright knot. In the bottom panel, the same X-ray contours are overlaid on the F658N image. The coincidence of the bright X-ray knot and the D31/32 optical emission is clearly seen. The outer contours closely follow the shape of the curved nonradiative filaments, albeit displaced slightly ($\sim 1''$). The outer contours also closely follow the faint nonradiative shocks to the north and to the west, which mark the limb of the remnant. The displacement between the X-ray and optical emission is probably due to a combination of the proper motion (or apparent proper motion) of the emitting features in the three years between the HST and *Chandra* observations and of some uncertainty in the registration of the images.

The observed properties of the D31/32 knots are well explained by a mechanism introduced by Jun et al. (1996) wherein Rayleigh-Taylor (R-T) fingers created at the contact discontinuity between the ejecta and swept-up ambient material are able to overtake the primary blastwave. The model requires the presence of a clumpy circumstellar medium where the rotational energy from vortices can be transferred to the R-T finger thereby increasing its velocity sufficiently for it to penetrate the forward shock. The protruding R-T finger will be rich in ejecta material and hence emit strongly in X-rays. Once the finger has overtaken the blast wave it will disrupt the so far "undisturbed" circumstellar medium and itself begin to be destroyed by R-T and Kelvin-Helmholtz (K-H) instabilities. The clumps generated in this interaction and mixing of the R-T finger and the circumstellar medium would then be shock excited by the primary blastwave. The time scales for this to happen are predicted by Jun et al. (1996) to be about 500 years for a "typical" SNR (see their Fig. 1).

The details of the evolution and ultimate fate of such R-T fingers are not well known. However, what is known matches our observations of Kepler remarkably well. The bright X-ray knot beyond the boundary of the remnant, the nonradiative shocks driven into the circumstellar medium, the fragmenting clumps from the interaction being shocked by the primary blastwave and radiating brightly in the optical are all basically predicted by the model, and they are happening on the expected time-scales. As Jun et al. (1996) point out, the random nature of the energy transfer from vortices to R-T fingers implies that not many such fingers will have enhanced growth that will allow them to overtake the forward shock. This is consistent with our observing just one such feature around the entire periphery of the Kepler SNR. Supporting evidence for this picture comes from the radio observations presented by DeLaney et al. (2002). The radio spectral index of the "bump" is -0.78 (see their Fig. 4). This is about the same as the spectral indices of other regions that they identify as shocked ejecta, and much steeper than those of regions dominated by the interstellar or circumstellar material.

The analysis of the X-ray emission will be crucial to understanding the physical processes that gave rise to the D31/32 knots and their emission. It would be important to know the composition of the bright X-ray knot to see if it is indeed composed of ejecta. This could possibly be accomplished with the 750 ksec *Chandra* observation of the Kepler SNR (PI: Reynolds). A second aspect of the X-ray observations that would be important is to measure the proper motion of the knot. Such a measurement would allow us to check if the velocity of the knot is consistent with its having originated as an R-T finger at the contact discontinuity and if so, to constrain when it was formed. We are undertaking analyses of multi-epoch *Chandra* data on Kepler, wherein this issue will be addressed (Ennis et al., in preparation).

5. Summary and Concluding Discussion

The optical images of the Kepler SNR presented here are the first reported in over a decade. The angular resolution of these images is about 20 times higher than any previously obtained, and therefore shows the structure of the emitting knots and filaments in unprecedented detail. In this paper, we have focused on a few issues where the small-scale structure revealed in these ACS images is of critical importance.

We have shown that fast nonradiative shocks and radiative shocks exist in sufficient proximity that ground based spectra sometimes cannot resolve them. This proximity of radiative knots and nonradiative filaments indicates that the pre-shock medium is highly clumped. We have also found that the [O III] to [N II] flux ratio is highly variable on small scales. Within a $\sim 24\ arcsec^2$ region there are sub-arcsecond knots where this ratio varies by almost an order of magnitude. The small-scale variation in ionization structure reflects differences in the shock velocities and also in the evolutionary stages of the post-shock emitting regions. The latter is clearly seen in the bright NW knots where the [O III] to [N II] decreases in knots further downstream from the primary shock front in the circumstellar cloud.

The remarkable complex of emission features around D31/32 is shown to consist of bright knots connected by faint, narrow filaments. The structure indicates that D31/32 was formed by a Rayleigh-Taylor or similar instability, as described by Jun et al. (1996). The complex is located just beyond the nominal perimeter of the remnant, as defined by the primary blastwave, and the optical emission coincides with a bright isolated X-ray knot. Based on these two facts, we conclude that the D31/32 feature has been formed by an R-T finger from the contact discontinuity between the forward and reverse shocks that has punched its way through the primary shock. This scenario deserves further scrutiny, necessarily using

multi-wavelength data and dynamical modeling.

It is clear from the images presented here that there still remains a wealth of information in these data. Our paper has concentrated on a few important issues where the high resolution data are immediately relevant, and which are almost entirely confined to the optical data. Other avenues of study include the overall distribution of knot sizes and brightnesses, and a comprehensive assessment of the time variability of the emission. A useful interpretation of the overall optical emission from Kepler will require taking into account the emission at other wavelengths. Fortunately a number of excellent datasets in the radio, IR and X-ray exist. Regarding the variability of the emission, the baseline between the HST/ACS data presented here and the last set of optical images is about 15 years, which is comparable to, and even exceeds the evolution time of the knots. Furthermore the difference in angular resolution is high and the relative flux calibrations between epochs is bound to be uncertain. Therefore obtaining meaningful results about the variation in the optical emission based just on existing data will be difficult. HST observations of the Kepler SNR in the future will be invaluable in characterizing changes in the optical emission.

We thank Steve Reynolds for making available the *Chandra* data for Kepler that were used in Fig. 10. We thank the referee for a number of useful suggestions that helped improve the paper.

Facilities: Hubble Space Telescope.

REFERENCES

Baade, W. 1943, ApJ, 97, 119

Bandiera, R. 1987, ApJ, 319, 885

Bandiera, R., & van den Bergh, S. 1991, ApJ, 374, 186

Blair, W. P., Long, K. S., & Vancura, O. 1991, ApJ, 366, 484 (BLV)

Blair, W. P., Ghavamian, P., Long, K. S., Williams, B. J., Borkowski, K. J., Reynolds, S. P., & Sankrit, R. 2007, ApJ, 662, 998

Borkowski, K. J., Blondin, J. M., & Sarazin, C. L. 1992, ApJ, 400, 222

Cassam-Chenaï, G., et al. 2004, A&A, 414, 545

Chevalier, R. A., Kirshner, R. P., & Raymond, J. C. 1980, ApJ, 235, 186

DeLaney, T., Koralesky, B., Rudnick, L., & Dickel, J. R. 2002, ApJ, 580, 914

Dennefeld, M. 1982, A&A, 112, 215

D'Odorico, S., Bandiera, R., Danziger, J., & Focardi, P. 1986, AJ, 91, 1382

Doggett, J. B., & Branch, D. 1985, AJ, 90, 2303

Fesen, R. A., Becker, R. H., Blair, W. P., & Long K. S. 1989, ApJ, 338, L13

Ghavamian, P., Raymond, J. C., Smith, R. C., & Hartigan, P. 2001, ApJ, 547, 995

Hartigan, P., Raymond, J., & Hartmann, L. 1987, ApJ, 316, 323

Hester, J. J., Raymond, J. C., & Blair, W. P. 1994, ApJ, 420, 721

Jun, B.-I., Jones, T. W., & Norman, M. L. 1996, ApJ, 468, L59

Koekermoer, A. M., Fruchter, A. S., Hook, R. N., & Hack, W. 2002, The 2002 HST Calibration Workshop. Edited by Arribas, Koekemoer and Whitmore. Baltimore, MD: Space Telescope Science Institute, p. 337

Minkowski, R. 1943, ApJ, 97, 128

Nahar, S. N. 1999, ApJS, 120, 131

Nahar, S. N., & Pradhan, A. K. 1997, ApJS, 111, 339

Raymond, J. C. 1979, ApJS, 39, 1

Reynolds, S. P., Borkowski, K. J., Hwang, U., Hughes, J. P., Badenes, C., Laming, J. M., & Blondin, J. M. 2007, ApJ, 668, L135

Sankrit, R., Blair, W. P., DeLaney, T., Rudnick, L., Harrus, I. M., & Ennis, J. A. 2005, Advances in Space Research, 35, 1027

Sollerman, J., Ghavamian, P., Lundqvist, P., & Smith, R. C. 2003, A&A, 407, 249

van den Bergh, S., & Kamper, K. W. 1977, ApJ, 218, 617

van den Bergh, S., Marscher, A. P., & Terzian, Y. 1973, ApJS, 26, 19

This preprint was prepared with the AAS LaTeX macros v5.2.

Fig. 1.— Hα+[N II] image of the Kepler SNR. The image is background- and star-subtracted and displayed with an arcsinh stretch to show the full intensity range. North is up and East to the left. The image dimensions are 200″× 187.5″. The numbered boxes highlight regions of emission for ease of reference.

Fig. 2.— Throughput as a function of wavelength for the F658N and F660N filters. The solid vertical lines indicate the positions of the Hα and [N II] λ6584 lines at zero velocity, and the dotted vertical lines the same at a velocity of -185 km s^{-1}.

Fig. 3.— The difference image between F658N and F660N emission, displayed so that nonradiative shocks are white and radiative shocks are black. Both F658N and F660N images were background subtracted. The scaling factor of 2.7 applied to the F660N image before subtracting was chosen for display purposes. The field of view is 45.0″ × 55.0″. North is up and east to the left. The inset is a 4.0″ × 3.25″ region showing the Balmer-dominated bow-shock feature. In the two-color image F658N is displayed in red and F660N is displayed in green (radiative shocks are therefore yellow). Both images have been background- and star-subtracted.

Fig. 4.— *(a)* F658N (red), and F660N (green) images of a 32.5″ square field of knots in the center-east of Kepler (left half of box 1 in Fig. 1). The images have been background- and star-subtracted. *(b)* Three color image of D49/D50, enlarged from the box shown in the left panel. F658N emission is shown in red, F660N emission in green and F550M continuum in blue. *(c)* Blow-up of a 3″× 3″region from the middle panel, showing a prominent [N II] knot. The knot has been so labeled. Also labeled are a star and an artefact that appear yellow in the image. As in Fig. 3, red features indicate pure Hα emission while yellow features indicate the presence of [N II] emission.

Fig. 5.— F658N (red), F660N (green) and F502N (blue) images of a 25.0″ × 17.5″ region near the center of the remnant. (Note that the blue channel in this color scheme differs from the one used in Fig. 4, while the red and green are the same.) Knots D41, 42, 44 and 45 are labeled. The images have been background- and star-subtracted. Balmer dominated emission appears red. Radiative knots with [N II] emission but no [O III] emission are yellow. Knots with both [N II] and [O III] emission are white. The faint bands towards the right of the image are due to the placement of the ACS/WFC chip gap during the observations. The exposure time on these regions is approximately half the total exposure time and hence the data are noisier than over the rest of the field of view.

Fig. 6.— Images of a 6.0″ × 4.5″ field in the region around D52 (box 7 in Fig. 1). The top panel is the F658N image displayed with an arcsinh stretch. The middle panel and bottom panels are the F660N and F502N images displayed with a linear stretch. The regions around

several knots selected for photometry are shown on the latter two images and are labeled on the F660N image. Note that region 5a is contained *within* region 5b. Several features identified as stars using the continuum image have been indicated with asterisks on the F660N image.

Fig. 7.— [N II] and [O III] emission from the bright NW knots (box 5 from Fig. 1). The left panel shows the F660N image in reverse grayscale (dark is brighter). The right panel shows $F_{[\mathrm{OIII}]}/F_{[\mathrm{NII}]}$ in reverse grayscale (dark is higher ratio). Both images are overlaid with contours obtained from the F502N image. The filter images were background subtracted. Stars were removed from the images by subtracting a suitably scaled continuum image. The field shown in $30'' \times 45''$.

Fig. 8.— ACS images of the D31/32 region. The top panel shows the F658N image, displayed with a linear stretch chosen to bring out the faint filaments. The bottom panel shows the F660N image. Both images are background- and star-subtracted, though some residuals remain at the positions of the stars. The field of view is $22.5'' \times 20''$, and north is up and east to the left. The region shown is in box 6 of Fig. 1.

Fig. 9.— Time evolution of the optical emission in the D31/32 region. The Hα+[N II] image obtained in 1987 (and first presented by BLV) is shown in red. The ACS F658N image, smoothed to the resolution of the ground-based data is shown in green. In the left panel, the data are displayed with an arcsinh stretch to highlight faint features. The display is linear in the right panel and emphasizes changes in the brighter regions. Some knots and features are labeled for ease of reference – see text for details. The field of view is about $32'' \times 32''$ (which is larger than that shown in Fig. 8), and north is up and east to the left.

Fig. 10.— X-ray and optical emission from the region around D31/32. The top panel shows X-ray contours overlaid on an X-ray image from *Chandra* (see text). The bottom panel shows the same X-ray contours overlaid on the ACS F658N image. The field of view is $50.6'' \times 40.5''$. North is up and east to the left.

Table 1. Summary of HST/ACS observations

Filter	Emission Lines	Observation IDs	Total exposure time (s)
F658N	Hα 6563Å + [N II] 6584Å	*j8pt01011,01021,01031,01041*	7459
F660N	[N II] 6584Å	*j8pt03011,03021,03031,03041*	4090
F502N	[O III] 5007Å	*j8pt02011,02021,03051,03061*	6220
F550M	line-free continuum	*j8pt02e6q,02enq,03nkq,03o4q*	840

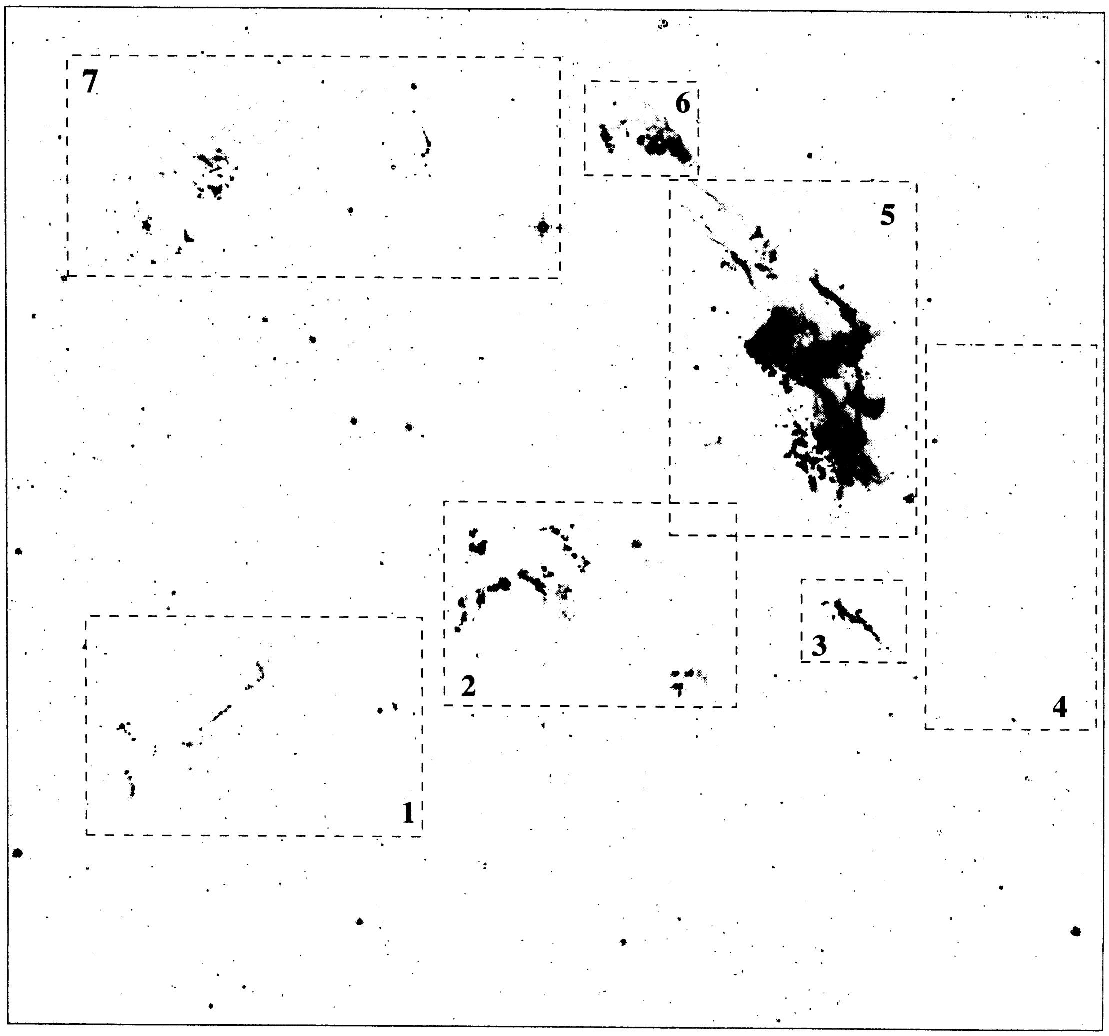
7
6
5
4
3
2
1

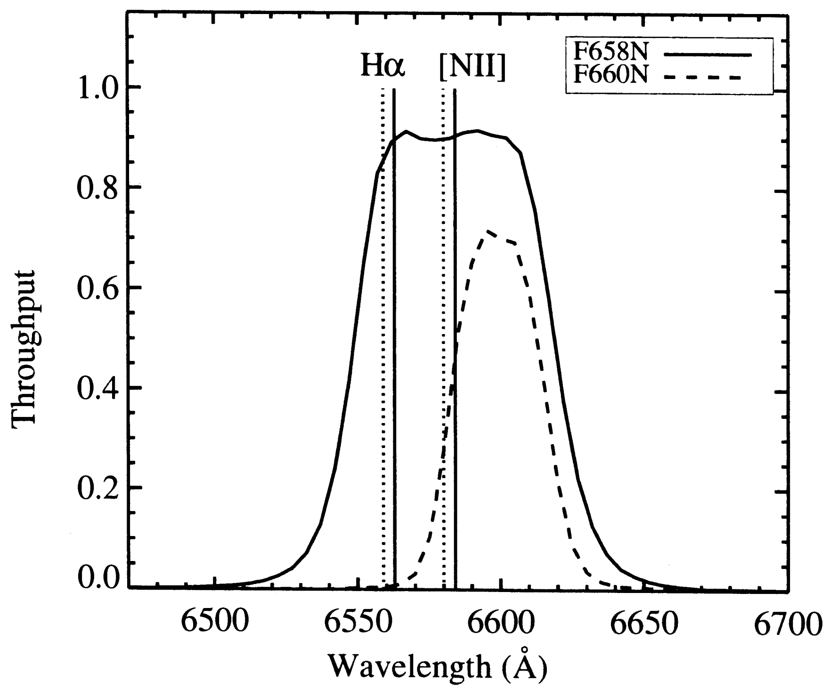
Hα
[NII]
F658N
F660N
1.0
0.8
0.6
0.4
0.2
0.0
Throughput
6500
6550
6600
6650
6700
Wavelength (Å)

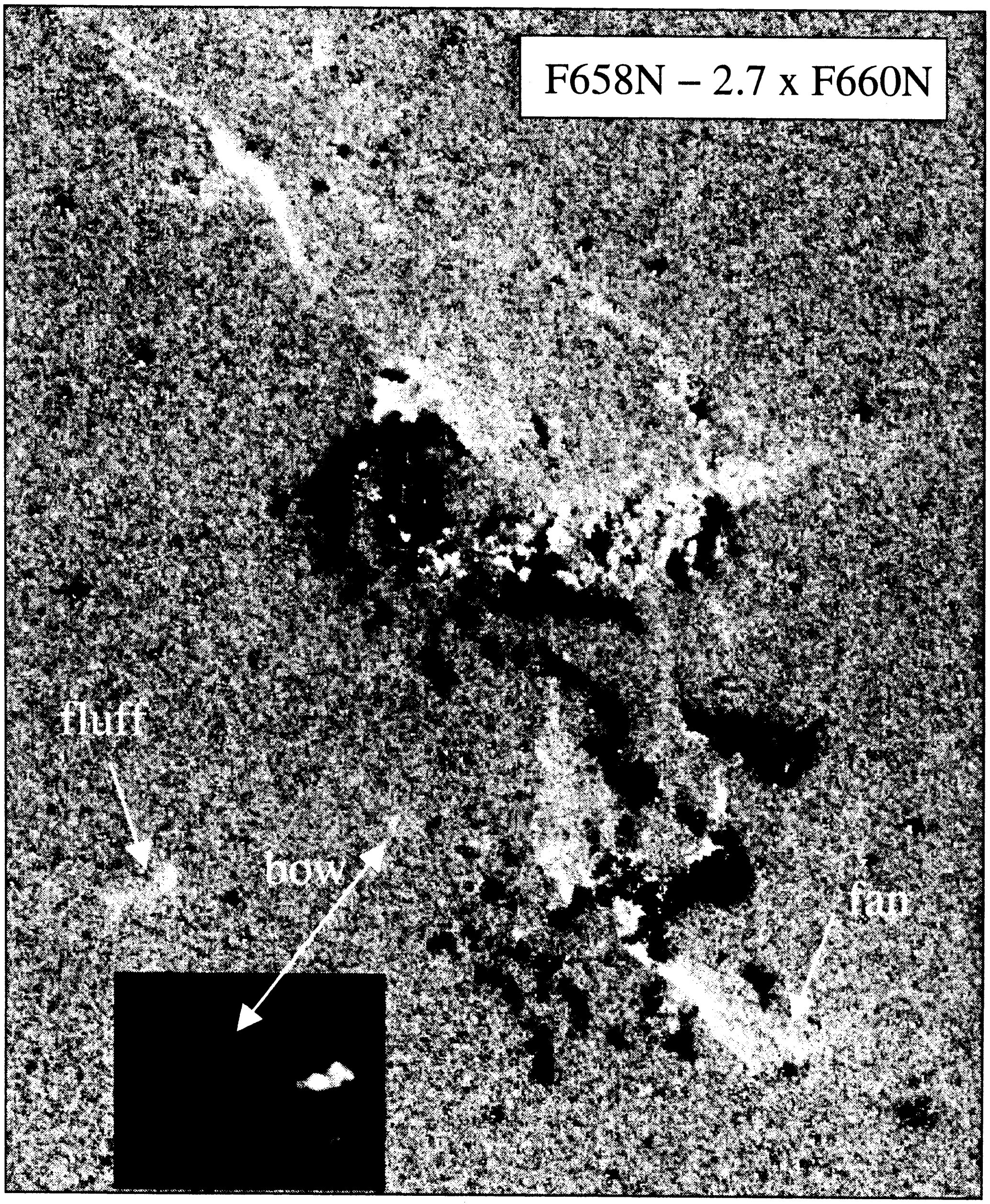
F658N – 2.7 x F660N
fluff
bow
fan

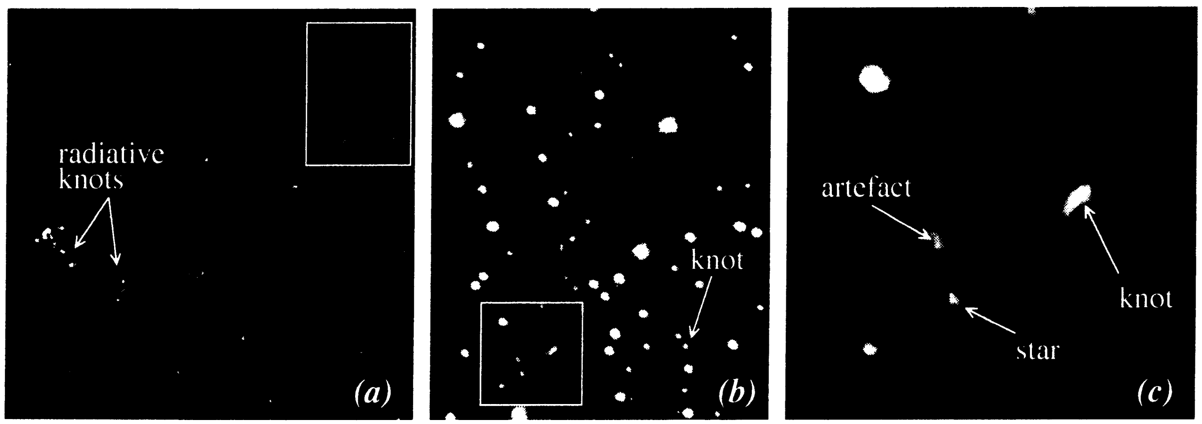
radiative
knots
(a)
knot
(b)
artefact
knot
star
(c)

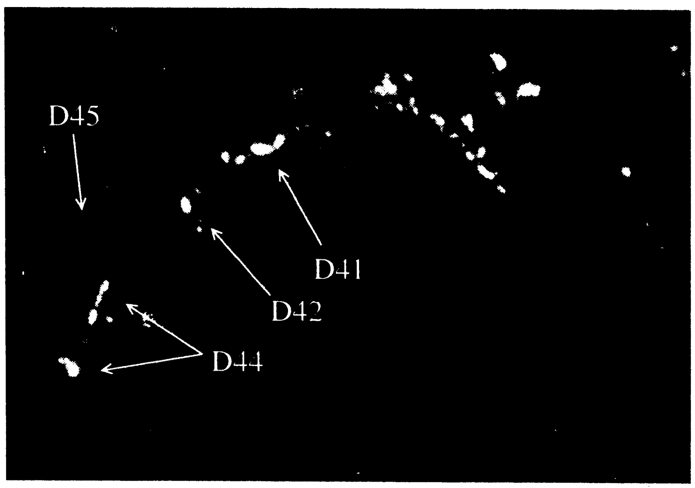
D45
D41
D42
D44

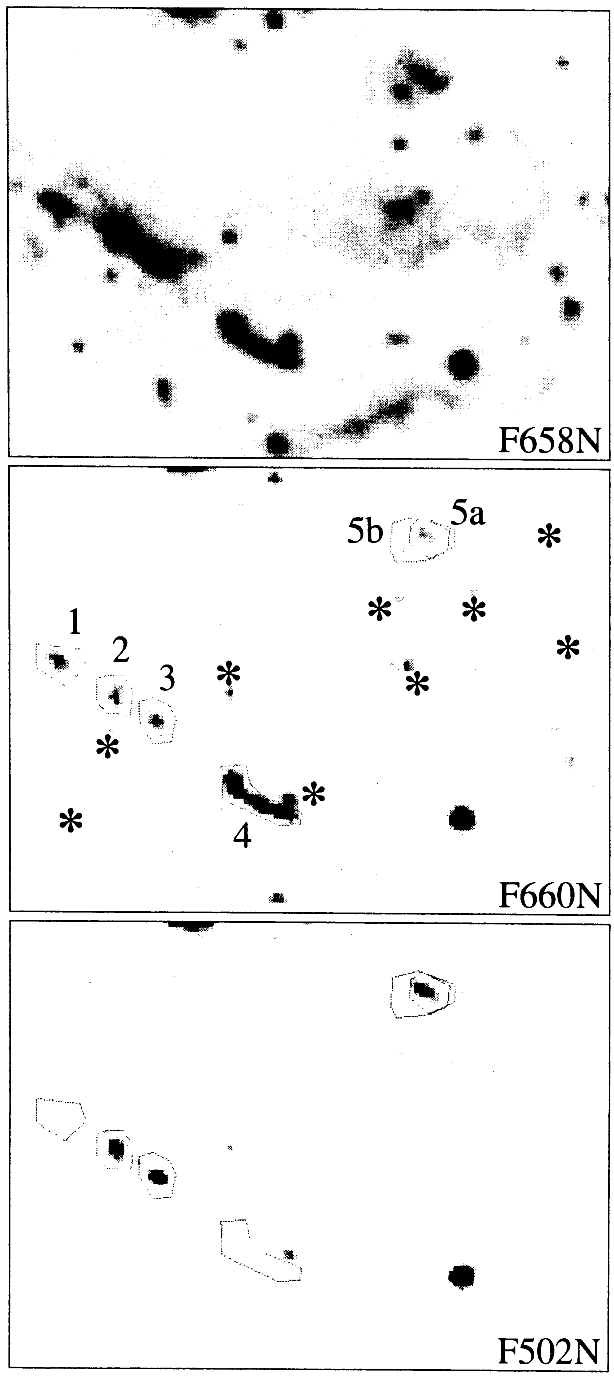
F658N
5b
5a
1
2
3
4
F660N
F502N

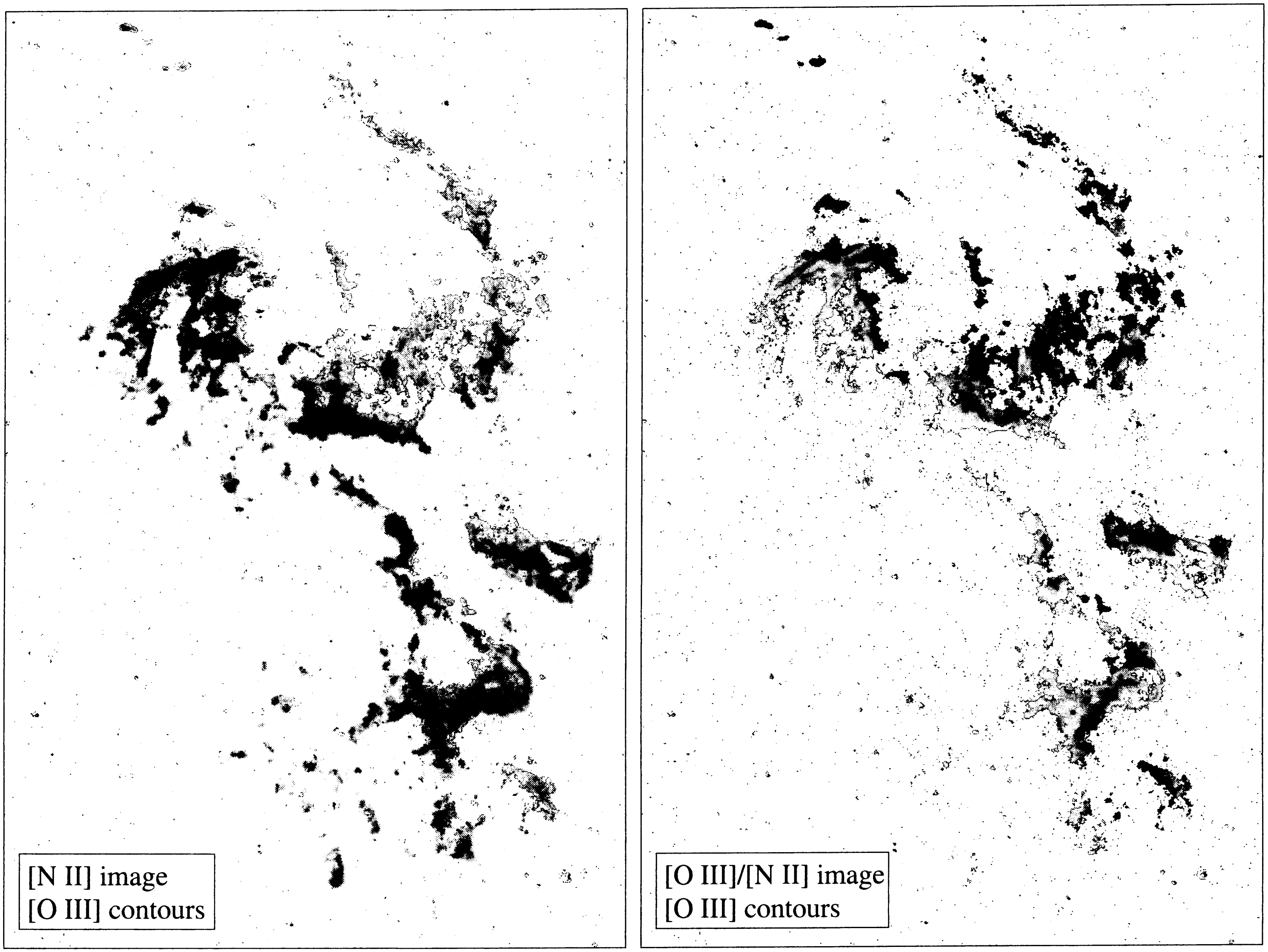
[N II] image
[O III] contours
[O III]/[N II] image
[O III] contours

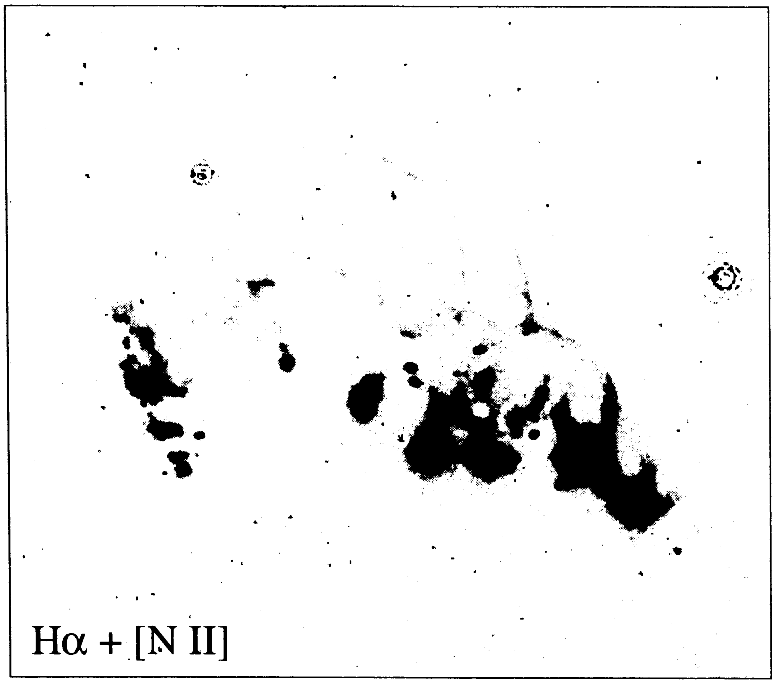
Hα + [N II]

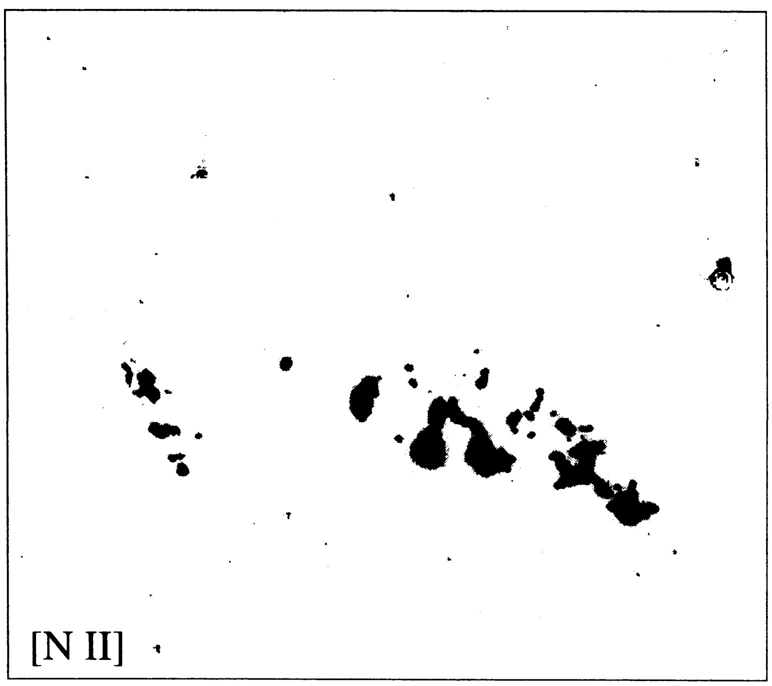
[N II]

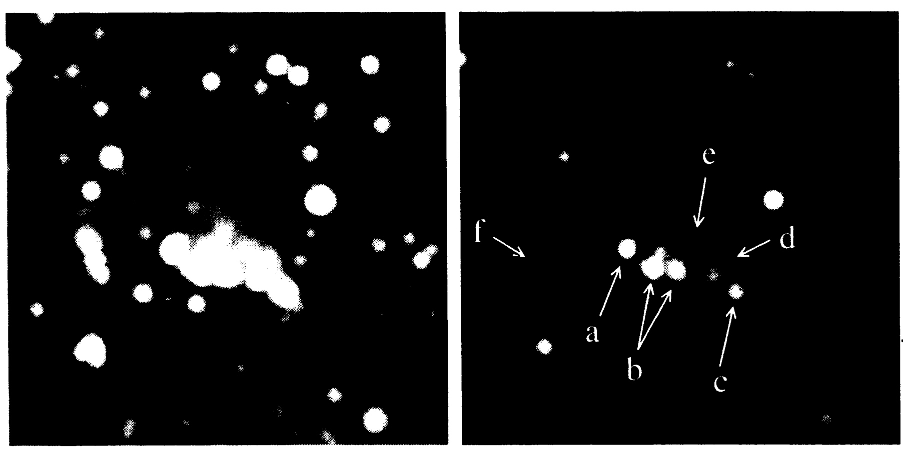
e
f
d
a
b
c

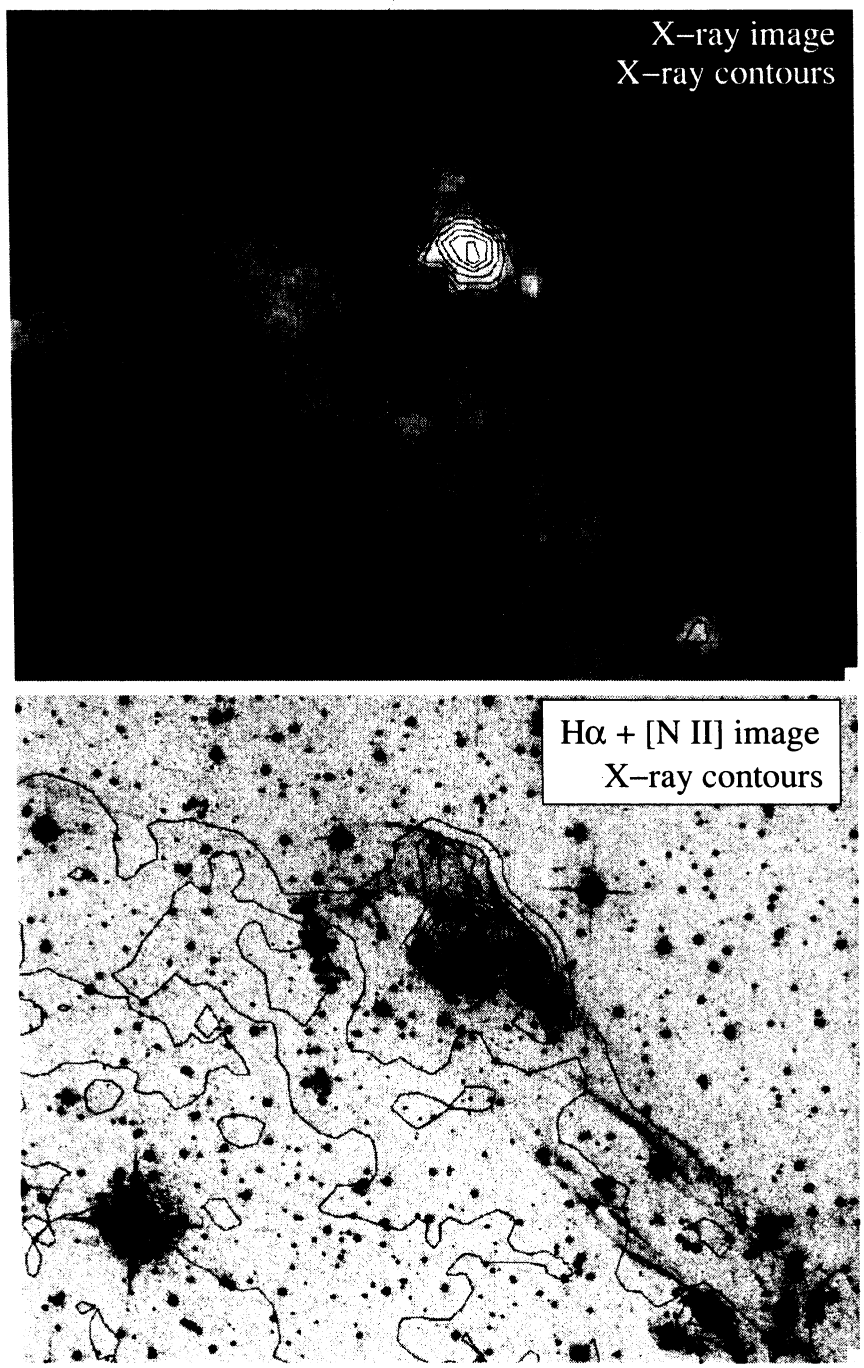
X–ray image
X–ray contours
Hα + [N II] image
X–ray contours